Volume 59
Number 79
11 October 2023
Pages 11743–11884

ChemComm

Chemical Communications

rsc.li/chemcomm

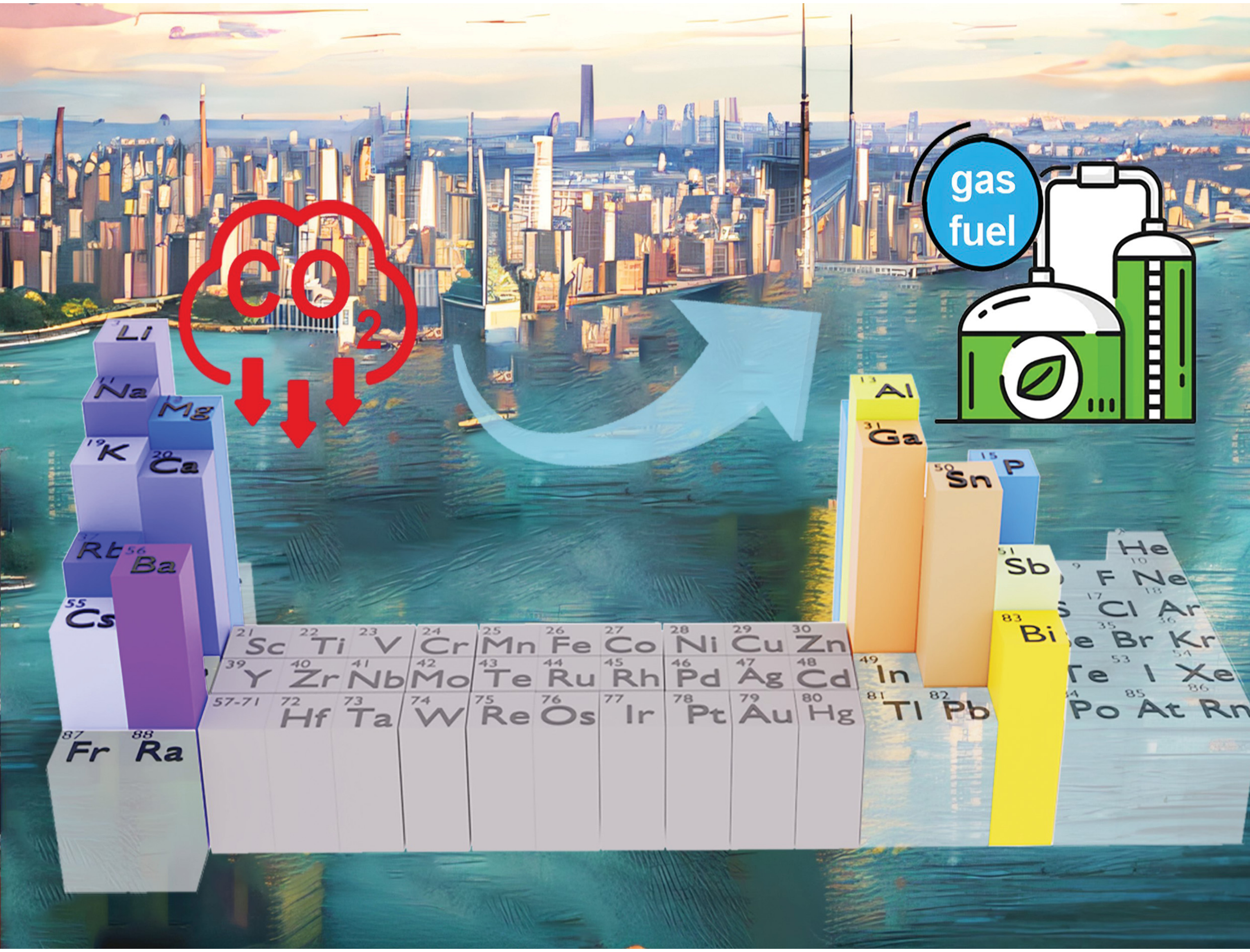

ISSN 1359-7345

ROYAL SOCIETY OF CHEMISTRY

FEATURE ARTICLE
Soumalya Sinha and Jianbing "Jimmy" Jiang
Main group elements in electrochemical hydrogen evolution and carbon dioxide reduction

ChemComm

FEATURE ARTICLE

View Article Online
View Journal | View Issue

Cite this: *Chem. Commun.*, 2023, **59**, 11767

Main group elements in electrochemical hydrogen evolution and carbon dioxide reduction

Soumalya Sinha and Jianbing "Jimmy" Jiang*

Main-group elements are renowned for their versatile reactivities in organometallic chemistry, including CO_2 insertion and H_2 activation. However, electrocatalysts comprising a main-group element active site have not yet been widely developed for activating CO_2 or producing H_2. Recently, research has focused on main-group element-based electrocatalysts that are active in redox systems related to fuel-forming reactions. These studies have determined that the catalytic performances of heavier main-group element-based electrocatalysts are often similar to those of transition-metal-based electrocatalysts. Our group has recently reported the scope of including the main-group elements in the design of molecular catalysts and explored their applications in redox catalysis, such as the generation of H_2 upon coupling of two protons (H^+) and two electrons (e^-). This feature article summarizes our research efforts in developing molecular electrocatalysts comprising main-group elements at their active sites. Furthermore, we highlight their influence on the rate-determining step, thereby enhancing the reaction rate and product selectivity for multi-H^+/multi-e^- transfer catalysis. Particularly, we focus on the performance of our recently reported molecular Sn- or Sb-centered macrocycles for electrocatalytic H_2 evolution reaction (HER) and on how their mechanisms resemble those of transition-metal-based electrocatalysts. Moreover, we discuss the CO_2 reduction reaction (CO_2RR), another promising fuel-forming reaction, and emphasize the recent progress in including the main-group elements in the CO_2RR. Although the main-group elements are found at the active sites of the molecular catalysts and are embedded in the electrode materials for studying the HER, molecular catalysts bearing main-group elements are not commonly used for CO_2RR. However, the main-group elements assist the CO_2RR by acting as co-catalysts. For example, alkali and alkaline earth metal ions (*e.g.*, Li^+, Na^+, K^+, Rb^+, Cs^+, Mg^{2+}, Ca^{2+}, and Ba^{2+}) are known for their Lewis acidities, which influence the thermodynamic landscape of the CO_2RR and product selectivity. In contrast, the elements in groups 13, 14, and 15 are primarily used as dopants in the preparation of catalytic materials. Overall, this article identifies main-group element-based molecular electrocatalysts and materials for HER and CO_2RR.

Received 26th July 2023,
Accepted 31st August 2023

DOI: 10.1039/d3cc03606e

rsc.li/chemcomm

Introduction

New findings for main-group element-based catalysts have changed the perception that main-group elements cannot behave similar to transition metals in catalysis. However, the development of electrocatalysts comprising main-group elements, particularly molecular electrocatalysts with a main-group element at the active center, is uncommon. The difference in the orbital energy levels is a challenge that renders it difficult for main-group element-based catalysts to compete with transition-metal-based catalysts. For main-group compounds, a high-energy gap exists in their valence s- or p-orbitals, whereas the valence d-orbitals in transition metals are relatively less energetic, which typically enables the transition-metal active site to interact with small molecular substrates (*e.g.*, CO_2, H_2, and O_2). Additionally, the valence s- or p-orbitals are often fully occupied, thus lacking vacant sites for the catalyst–substrate interactions. However, heavier main-group elements, such as Al, Sn, and Sb, have larger covalent radii than their lighter counterparts, such as B, C, and N, and can attain higher coordination numbers in their complexes. Consequently, the inclusion of heavier main-group elements has gained recognition in catalyst design for small-molecule activation.[1] Moreover, elements in Groups 1 and 2 have been influential in multi-proton (H^+) and multi-electron (e^-) redox catalysis, and typically promote catalysis by enhancing reaction kinetics.[2–4]

Molecular electrocatalysts are great platforms to understand the structure–function relationship, but the current research desires more catalytic materials upon immobilizing the molecular catalyst. Although strategies to immobilize molecular catalysts on the electrode surface have been reported,[5,6] molecular catalysts bearing main-group elements at the active center

---

Department of Chemistry, University of Cincinnati, P.O. Box 210172, Cincinnati, Ohio 45221, USA. E-mail: jianbing.jiang@uc.edu

are rarely known. The applications of main-group complexes in molecular electrocatalysis are also rare. Recently, our group has sought to include main-group elements in the design of molecular electrocatalysts. For example, we have reported molecular Sn- or Sb-centered macrocycles that couple multi-H^+ and multi-e^- to generate H_2 electrocatalytically.[7,8] We have also investigated the electrochemical mechanism of these Sn or Sb complexes toward the H_2 evolution reaction (HER), supported by computational calculations. This article includes our contributions toward the design of main-group element-centered electrocatalysts and their performance in the electrocatalytic HER. Furthermore, we emphasize the work of others in the electrocatalytic HER using main-group elements to highlight recent progress in this field.

We believe that main-group element-based electrocatalysts could be promising for the efficient CO_2 reduction reaction (CO_2RR). Finding robust and efficient CO_2RR catalysts has been of great interest, owing to their ability to mitigate atmospheric CO_2.[9–11] However, most catalyst designs rely on transition metals. In 2010, Ménard and Stephen reported that CO_2 could be reduced to methanol (CH_3OH) using an $(Mes)_3P(CO_2)(AlX_3)_2$ complex, where Mes is a mesitylene group and X is a bromide or chloride.[12] They revealed that Al-based frustrated Lewis pairs (FLP) are the important factors in CO_2RR chemistry. Inspired by these results, several FLP-based main-group complexes have been explored for the CO_2RR, and the most common product observed was formate (HCO_2^-).[13] Another example of the electrochemical CO_2RR using main-group-based FLP was reported by Thompson and Heiden, where an FLP supported CO_2 insertion into a main-group hydride bond while reducing CO_2 electrochemically.[14] They also investigated the effects of Lewis acids on the reactivity of CO_2 insertion into the main-group hydride bond by comparing the activities of seven Lewis acids, $[PhSiH_2]^+$, $[SiEt_3]^+$, $B(C_6F_5)_3$, $B(C_6F_5)_2Ph$, $B(C_6F_5)Ph_2$, BPh_3, and BEt_3, where Ph and Et denote phenyl and ethyl groups, respectively. The authors noted that stronger Lewis acids, such as $B(C_6F_5)_3$, became poor hydride donors to CO_2 upon forming a metal–hydride bond, such as $[HB(C_6F_5)_3]^-$. Furthermore, Lewis acids from Groups 1 and 2, as well as transition-metal-based catalysts, assisted in controlling the CO_2RR selectivity and kinetics under electrochemical conditions, and we include this discussion later. In addition to the Lewis acid effects of the main-group elements, we highlight examples wherein they act as dopants when incorporated into electrode materials for the CO_2RR. Overall, this article presents examples of the main-group element-assisted electrochemical HER and CO_2RR, including recent reports from our group.

Main group elements at catalytic site

To our knowledge, extremely few main-group elements serve as the active sites of catalysts for the electrochemical HER or CO_2RR. Al, Ga, Sn, Sb, and Bi have been used as catalyst active sites while performing electrochemical HER. To date, no main-group elements have been explored as the active center of the electrocatalyst for CO_2RR. In this section, we focus only on the main-group elements used as molecular HER electrocatalysts and summarize their roles in the electrochemical mechanisms.

Al. The second element in group 13, Al has rarely been used in electrocatalysis, except for two unique examples of Al(III) complexes that promote the HER, as reported by Berben *et al.*[15,16] They synthesized two Al(III) complexes chelated with a redox-active ligand, phenyl-substituted bis(imino)pyridine (**Al-BIP**, Fig. 1(A)) or bis(pyrazolyl)pyridine (**Al-BPP**, Fig. 1(B)), and studied their activities for H_2 production. The electrochemical HER studies were performed by dissolving these Al(III)

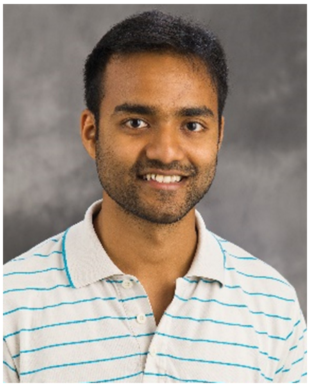

Soumalya Sinha

Soumalya Sinha was first introduced to electrochemistry as a graduate student at Simon Fraser University, where he worked with Prof. Jeff Warren. A key aspect of his PhD study was investigating how catalysts with proton relays behave on solid electrodes. As a postdoctoral research fellow at the University of Illinois–Urbana Champaign, he investigated the electrocatalytic hydrogen evolution reaction using bioinspired catalysts. In 2021, Soumalya joined the Department of Chemistry at the University of Cincinnati as a visiting assistant professor, and his current research interests lie in electrochemical small molecule activation.

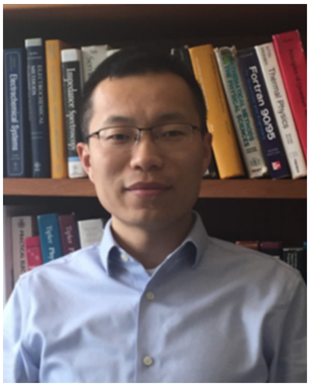

Jianbing "Jimmy" Jiang

Jianbing "Jimmy" Jiang is currently an Associate Professor in the Department of Chemistry at the University of Cincinnati. Dr Jiang earned his BS from Jiangnan University in 2007 and MS from East China University of Science and Technology in 2010, working with Dr He Tian. He obtained his PhD from North Carolina State University (advisor: Jonathan Lindsey) working on tetrapyrrole compounds for energy applications. In 2015, he joined Yale University as a Postdoctoral Associate and then became an Associate Research Scientist in the Department of Chemistry and Yale Energy Sciences Institute, working with Professors Gary Brudvig and Robert Crabtree on organometallic materials for small molecule activation and energy storage. His current research focuses on electrocatalysis and electrochemical energy storage.

complexes in tetrahydrofuran (THF) with a tetrabutylammonium hexafluorophosphate (^{n}Bu$_4$NPF$_6$) electrolyte in the presence of a Brønsted acid, which supplied multiple H$^+$. Under these electrochemical conditions, a faradaic efficiency (FE) of 85% for H_2 production was observed using **Al-BIP** in the presence of 4-dimethylaminopyridinium (HDMAP$^+$, 20 equiv.) by performing controlled potential electrolysis for 1.5 h at an overpotential of 0.5 V. The electrochemical HER mechanism of **Al-BIP** was also studied, and it was proposed that two sequential proton transfers first occurred at the ligand center (Fig. 1(A)). The protonated **BIP** ligand (by 2H$^+$) in **Al-BIP** underwent two further sequential 1e$^-$ reduction steps to generate H_2 (Fig. 1(A)).

A similar electrochemical HER performance was observed for **Al-BPP** using triethylammonium ([HNEt$_3$]$^+$) or salicylic acid as the proton source in the THF electrolyte;[16] however, **Al-BPP** followed a slightly different electrochemical HER pathway (Fig. 1(B)). The **BPP** ligand in **Al-BPP** was first reduced by 1e$^-$, and a proton-coupled electron transfer step occurred at the **BPP** ligand. Finally, 1H$^+$ reduction generated H_2 (Fig. 1(B)). Detailed electrochemical data analysis revealed that Al(III) did not participate in H$^+$ and e$^-$ transfer events. The supported redox-active ligand underwent sequential H$^+$/e$^-$ reduction to form a ligand-based hydride intermediate, which released H_2 in the presence of acids in the solution. Notably, both HER pathways promoted by **Al-BIP** and **Al-BPP** proceeded without forming any typical metal–hydride intermediates, which is common in transition-metal-centered HER electrocatalysts.[17–19] Overall, this research effort inspired a main-group-based molecular electrocatalyst design for HER catalysis.

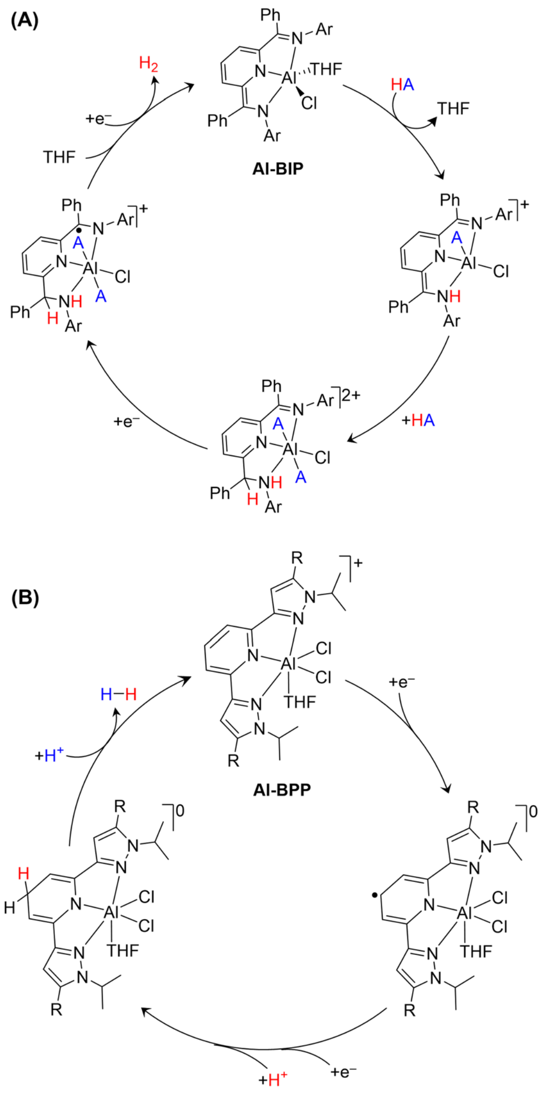

Fig. 1 Two different electrochemical HER pathways promoted by Al(III) complexes, (A) **Al-BIP** and (B) **Al-BPP**, coordinated with a redox-active ligand. HA is HDMAP$^+$. Adapted with the permissions of ref. 15 and 16.

Ga. Cao *et al.* reported a remarkable HER using Ga(III) chloride tetrakis(pentafluorophenyl)porphyrin (**ClGa^{III}TPF$_5$**, Fig. 2(A)).[20] In their study, the authors proposed that a Ga(III) porphyrin derivative promoted H_2 production, where the ligated porphyrin was first reduced consecutively by 2e$^-$, followed by a Ga(III)–hydride species formation (Fig. 2(B)) using H$^+$ from the added acid source, 2,2,2-trifluoroacetic acid (TFA). A signal at −6.45 ppm in the ^{1}H NMR spectrum confirmed the

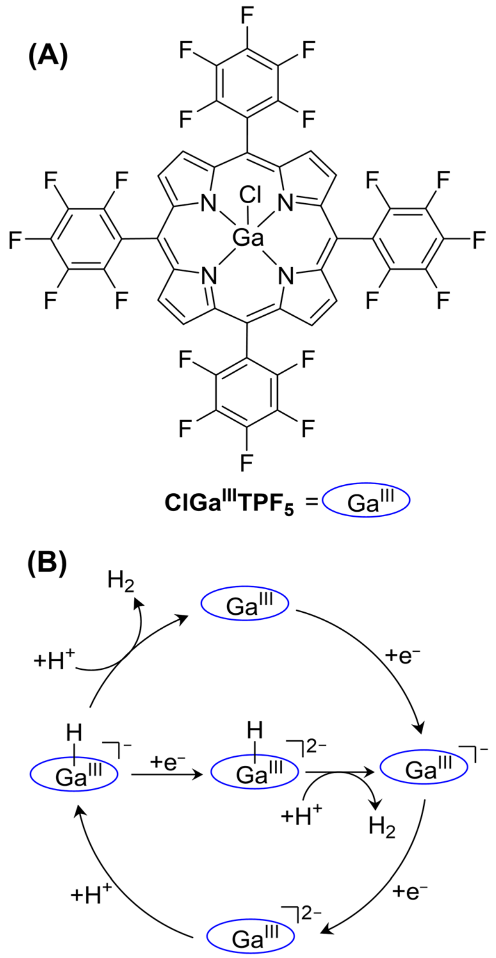

Fig. 2 (A) Ga(III) chloride tetrakis(pentafluorophenyl)porphyrin studied for electrochemical HER and (B) its mechanism for producing H_2 *via* a Ga–hydride intermediate. Adapted with the permission of ref. 20.

formation of the Ga(III)–hydride intermediate. In addition to NMR spectroscopy data, UV-visible spectroscopic studies were also carried out for the further detection of $1e^-$ or $2e^-$ reduced species of **$ClGa^{III}TPF_5$**. Interestingly, a weak absorption band between 560–700 nm appeared when Ga^{III}–hydride species was formed after the reaction between $2e^-$ reduced **$ClGa^{III}TPF_5$** species and added acids (AcOH or TFA). Furthermore, such experiments also supported the hypothesis that protonation events during the HER process take place at the Ga^{III} center rather than at the *meso*-position of the porphyrin ring. Finally, further protonation of the Ga(III)–hydride intermediate using Brønsted acids resulted in H_2 production. A turnover frequency (TOF) of $9.4 \times 10^4\ s^{-1}$ was estimated for the HER using this molecular Ga(III) porphyrin catalyst in CH_3CN with TFA (97 equiv.). Moreover, the HER kinetics observed using this Ga(III) porphyrin catalyst were much higher than those of the Sb(III)-porphyrin-derived catalysts. This phenomenon could be rationalized by considering the stronger hydride-donating ability of the Ga(III)-based hydride than that for the Sb(III)-based hydride, owing to the smaller electronegativity of Ga.[20]

Sn. Motivated by the performance of Ga(III) and Sb(III) porphyrins toward electrochemical HER, we recently reported an asymmetric PEGylated Sn(IV) porphyrin (**$Cl_2Sn^{IV}PEGP$**, Fig. 3(A)) for homogeneous HER in a non-aqueous electrolyte.[8] **Cl_2Sn^{IV}-PEGP** was prepared by refluxing PEGylated porphyrin ligand with excess amount (10 equiv.) of $SnCl_2{\cdot}2H_2O$ in anhydrous pyridine for 3 h. Treating the reaction mixture with citric acid, followed by the extraction in CH_2Cl_2 yielded the crude product, which was purified using the column chromatography. The yield of **Cl_2Sn^{IV}-PEGP** was 81% and the purity of the final product was confirmed using typical spectroscopy techniques, such as NMR, UV-visible, and ESI-MS.

$Cl_2Sn^{IV}PEGP$ exhibited a high catalytic current density ($4.6\ mA\ cm^{-2}$) with an FE of 94% for H_2 production.[8] The TOF was $1099\ s^{-1}$ in the presence of 16 mM TFA as the proton source. Spectroelectrochemical analysis and density functional theory (DFT) calculations revealed that this Sn–porphyrin catalyst followed an ECEC pathway for the HER, where E and C denote e^- and H^+ transfer events, respectively. Cyclic voltammetry data also supported the HER mechanism. In brief, a reductive wave at −0.8 V with a small (∼0.01 mA) peak current was observed upon adding TFA in the bulk electrolyte solution. The peak potential of such a cathodic wave started to shift toward more positive potentials as the TFA concentration was increased, suggesting the protonation step at the Sn center. Furthermore, the ''peak-shift'' analysis with the logarithm of TFA concentration revealed a Nernstian EC step at the beginning of the electrochemical mechanism, also in good agreement with the DFT data. In brief, **$Cl_2Sn^{IV}PEGP$** was first reduced by $2e^-$ to form **$Sn^{II}PEGP$**, which proceeded *via* the ECEC mechanism to generate the Sn(IV)PEGP–hydride species, **$Sn^{IV}H$-INT1** (Fig. 3(B)). We confirmed the generation of **$Sn^{IV}H$-INT1** by reporting an ^1H NMR signal at −0.9 ppm, which is attributed to the Sn(IV)–H species. Moreover, we proposed that **$Sn^{IV}H$-INT1** was further reduced by $1e^-$ to **$[Sn^{IV}H\text{-INT1}]^-$**. The second protonation of **$[Sn^{IV}H\text{-INT1}]^-$** generated an Sn(II)–PEGP–H_2 intermediate (**$Sn^{II}H_2$**), which released H_2 as the product. Overall, this is a novel example of an Sn-based molecular electrocatalyst that generates H_2 in a non-aqueous medium.

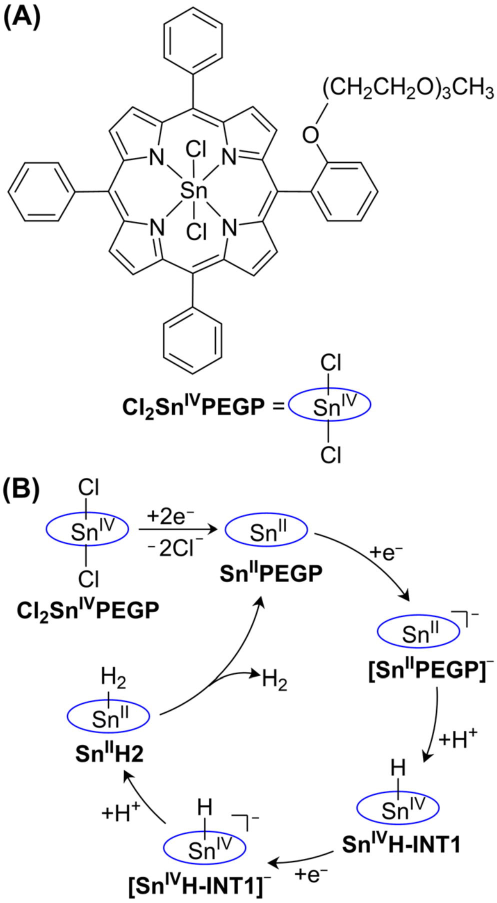

Fig. 3 (A) Sn porphyrin and (B) its electrochemical mechanism for the HER in a non-aqueous electrolyte. Adapted with the permission of ref. 8.

In addition to our reported molecular Sn(IV) electrocatalyst, Sn-doped MoS_2 electrodes have been studied for their electrochemical HER activity.[21] A previous study reported a synthesized multilayered MoS_2 with Sn dopants, and spectroscopic methods were employed to characterize the materials. These materials performed the HER over 12 h at a current density of $10\ mA\ cm^{-2}$ in an aqueous electrolyte.

Sb. Sb macrocycles, such as Sb porphyrin[22] and Sb salen[7] complexes, have been studied for their electrochemical HER activities. Brudvig *et al.* investigated a series of Sb(V) porphyrins and determined that a 5,10,15,20-tetra(*p*-tolyl)porphyrin ligand chelating with an Sb(V) center (**$TPSb(OH)_2$**, Fig. 4(A)) is a promising molecular HER electrocatalyst in a non-aqueous electrolyte.[22] Notably, both the porphyrin ligand and Sb metal center were redox active during the electrocatalytic HER, which is rarely observed for Sb-based catalysis. Furthermore, bulk electrolysis performed over 2 h using **$TPSb(OH)_2$** showed a stable catalytic current owing to the HER, with an FE of 62% for H_2. Mechanistic insights into the HER catalyzed by

TPSb(OH)$_2$ were also obtained using DFT calculations. Two consecutive ligand-centered reductions coupled with a single H^+ transfer eliminated one molecule of water and generated a Sb(III) porphyrin derivative (**TPSb^{III}**, Fig. 4(B)). These **TPSb^{III}** species then underwent a CEC pathway, where C and E denote H^+ and e^- transfers, respectively, to generate the **TPSbH$_2$** species *via* two consecutive intermediates, **TPSbH-INT1** and **TPSbH-INT2**. Finally, **TPSbH$_2$** released H_2 and returned to **TPSb^{III}** *via* the intermediate **TPSb^{IV}**. The free energy change (ΔG) associated with the step from **TPSbH-INT2** to **TPSbH$_2$** was 3.2 kcal mol^{-1}, with a ΔG activation at 16.2 kcal mol^{-1}. Furthermore, the H–H bond length in **TPSbH$_2$** was 0.76 Å, which is similar to that in an isolated H_2 molecule. Additionally, the distance between Sb and H_2 in the **TPSbH$_2$** intermediate was 3.3 Å, indicating a weak interaction that could ease the release of H_2 as the final product.

Motivated by the activity of **TPSb(OH)$_2$** in the electrochemical HER, we recently developed a Sb(III) salen complex (**SbSalen**, Fig. 5) and reported its activity toward the electrochemical HER by immobilizing it onto C-paper working electrodes.[7] **SbSalen** complex was synthesized by stirring 2.5 equiv. of triethylamine and 1 equiv. of salen ligand in dry CH_2Cl_2 for 25 min, followed by the addition of $SbCl_2$ (1 equiv.) at 0 °C under the O_2-free condition. Further stirring for 24 h yielded a yellow suspension which was filtered and thoroughly washed with CH_2Cl_2 and hexane to obtain pure **SbSalen** in ~70% yield.

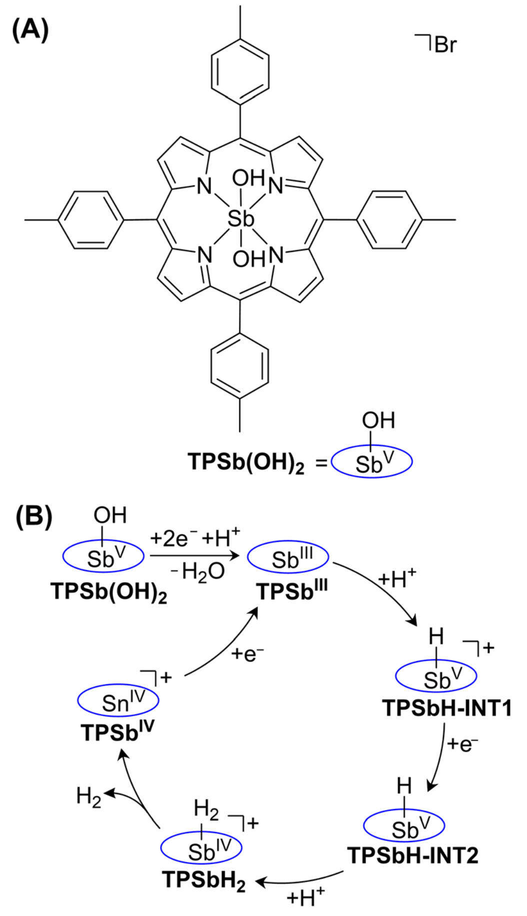

Fig. 4 (A) Sb(V) porphyrin, **TPSb(OH)$_2$**, and (B) its mechanism for electrochemical HER in a non-aqueous electrolyte. Adapted with the permission of ref. 22.

In an aqueous medium, we observed a high catalytic current of 30 mA cm^{-2}, with a TOF of 43.4 s^{-1} using **SbSalen**. Furthermore, DFT calculations revealed that the electrochemical HER mechanism was promoted by the **SbSalen** complex, which underwent the ECEC pathway (Fig. 5). Notably, the protonation of **SbSalen** for these C steps occurred at the O or N atom of the salen ligand, not at the Sb center. Moreover, once both the O and N atoms were protonated at the end of the ECEC steps, the H atom attached to the O atom was transferred to the Sb center and formed an Sb(III)–hydride species. Our computational calculations supported this H-atom transfer from the O atom to the Sb center, because the kinetic barrier of bond dissociation was less for the O–H bond (0.28 eV) than that for the N–H bond (0.49 eV). However, these Sb(III)–hydride species released molecular H_2 as a product and returned to the resting state of the **SbSalen**. Moreover, **SbSalen** produced H_2 with 100% FE in an aqueous medium, which is a unique example of an Sb electrocatalyst for the HER. The stability of **SbSalen** immobilized onto the C-paper was tested over 3 h, and further studied using X-ray photoelectron spectroscopy (XPS). The XPS data revealed that no demetallation event occurred during the electrolysis. Additionally, no change in the oxidation state of Sb was observed upon the completion of the catalysis, indicating the overall molecular integrity of the catalyst throughout the electrochemical HER process.

Bi. Bi as the active center of Bi-based molecular HER electrocatalysts is rare, except for an example reported by Luo *et al.*[23] They successfully synthesized a Bi complex that chelated with an NCN-type pincer ligand (**(NCN)Bi(III)**, Fig. 6(A)) for proton reduction under weakly acidic conditions.[23] This study

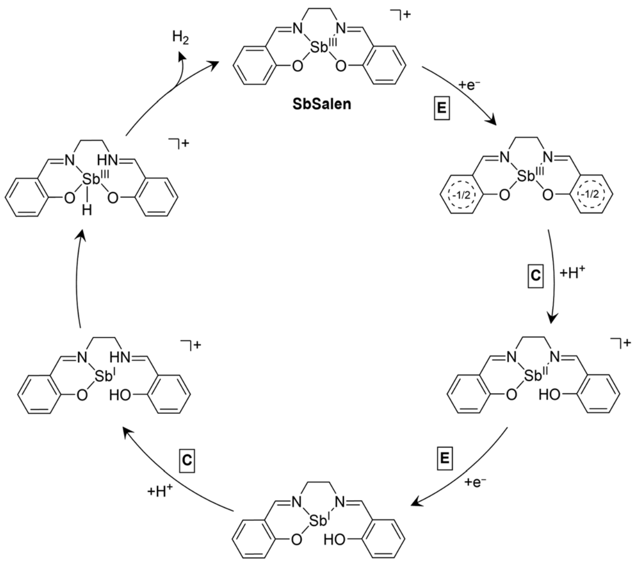

Fig. 5 **SbSalen** complex and its promoted ECEC mechanism for the HER. Adapted with the permission of ref. 7.

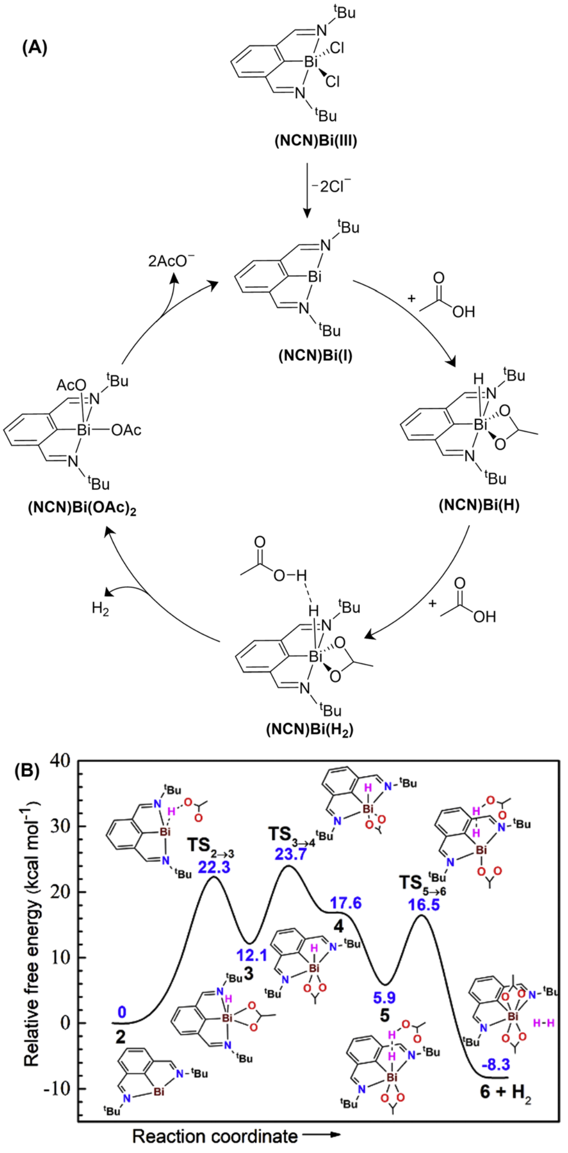

Fig. 6 (A) Molecular Bi(III) HER electrocatalyst and (B) energy profile for its promoted HER pathway. Adapted with the permission of ref. 23.

reported that the HER mechanism involved the generation of a low-valent Bi(I) complex (**(NCN)Bi(I)**) that was reactive toward weak acids (Fig. 6(A)). At the beginning of the Bi-catalyzed HER in the presence of AcOH, **(NCN)Bi(III)** was reduced by 2e⁻ to form **(NCN)Bi(I)**, which formed a six-coordinated Bi–hydride species that chelated with AcOH, **(NCN)Bi(H)**. These Bi–hydrido species underwent a series of configuration changes before interacting with the second molecule of AcOH (Fig. 6(B)). The coordination of the second AcOH molecule protonated the Bi–hydrido species and generated H_2 molecules *via* the intermediate **(NCN)Bi(H₂)**. Finally, the intermediate **(NCN)Bi(OAc)₂** was formed and returned to the **(NCN)Bi(I)** complex to complete the cycle. A detailed investigation of the DFT calculations determined the transition state structures and energy profiles (Fig. 6(B)), where the release of H_2 at the final stage of the catalytic cycle was thermodynamically favorable.

Table 1 Comparative electrochemical performance of main-group-based molecular HER electrocatalysts

Catalyst	Solvent	Turnover frequency (s^{-1})	Overpotential (V)	Faradaic efficiency (%)
Al-BIP	THF	1.1×10^{-4}	0.54	85
ClGaTPF₅	MeCN	9.4×10^{4}	~1.0	97
Cl₂SnPEGP	MeCN	1.1×10^{3}	0.9	94
TPSb(OH)₂	MeCN	1.2×10^{-3}	0.6	62
SbSalen[a]	H_2O	43.4	1.4	~100
(NCN)Bi(III)	MeCN	$\sim 1.8 \times 10^{3}$	0.69	88

[a] Immobilized onto carbon paper electrodes.

The performance of the main-group-based electrocatalysts toward HER such as turnover frequency, overpotential, and faradaic efficiency have been tabulated in Table 1 and also shown in Fig. 7(A)–(C). Besides molecular electrocatalysts, inorganic materials comprising the transition metal and main-group elements, especially phosphides have been explored for the production of H_2.[24,25] Noteworthy, the electrocatalytic HER promoted by Ni_xP_y materials was impressive as their performance was comparable to the most efficient Pt-based materials. The morphologies of such inorganic materials containing various transition metals and phosphides are shown in Fig. 7(D).[24]

Main group element assisted HER

Main-group elements often assist in the electrochemical HER rather than acting as active sites of the catalysts. In particular, the presence of main-group elements enhances HER kinetics by acting as co-catalysts. In this section, we briefly highlight examples and discuss roles of the main-group elements in the HER.

Ge. Ge can be used as an electrode in the HER and forms Ge hydroxide (Ge–OH) functionalities when the electrodes are anodically polarized. In 1960, Gerischer *et al.* proposed that Ge–OH electrodes can react with $1H^+$ and $1e^-$ to generate Ge radicals on the surface, with H_2O as a product.[26] The Ge radicals formed Ge hydride (Ge–H) in the presence of H^+, and a further reduction with $1H^+$ and $1e^-$ produced H_2. Memming and Neumann supported Ge electrode-promoted HER mechanisms using cyclic voltammetry (CV) data.[27] They further determined that the formation of Ge radicals and Ge–H species on the electrode surface was potential-dependent and could be controlled by tuning the potential window while cathodically scanning. In addition, they reported that the number of electrons in the conduction band at the electrode surface determined the electron-transfer kinetics, which could be enhanced by applying more negative potentials to the cathode.

Bi. The effects of Bi on Pb electrodes were investigated for HER in an H_2SO_4 solution.[28] Less than 0.733 wt% Bi was added to the commercially purchased Pb to generate the Bi–Pb alloys, which were deposited onto the pure Pb electrodes. By varying the Bi content, the authors demonstrated that the HER rate depended on the Bi loading; thus, a higher Bi content resulted in higher HER kinetics.

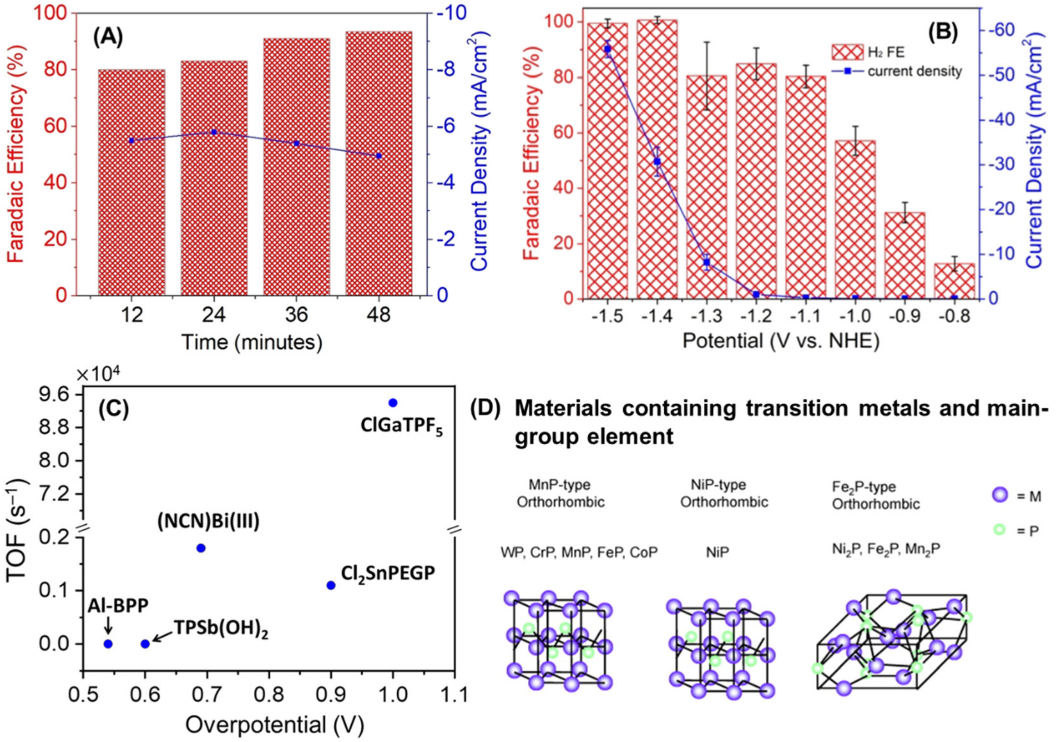

Fig. 7 Faradaic efficiencies and current densities observed for (A) **$Cl_2SnPEGP$** under homogeneous and (B) **SbSalen** under heterogeneous conditions for the electrochemical HER. Adapted with the permission of ref. 8 and 7. (C) Benchmarking the maximum turnover frequencies and overpotentials for reported molecular HER electrocatalysts, **Al-BPP**, **$TPSb(OH)_2$**, **(NCN)Bi(III)**, **$Cl_2SnPEGP$**, and **$ClGaTPF_5$**. (D) Inorganic materials containing transition metals and phosphide for efficient electrochemical HER. Adapted and slightly modified with the permission of ref. 24.

Main group element assisted CO_2RR

The main-group elements that serve as the active sites of molecular electrocatalysts for CO_2RR are not yet known. The effects of the main-group elements in assisting the CO_2RR, either as promoters or dopants, have been well explored. In particular, metals in groups 1 and 2 are effective in enhancing the reaction kinetics, product selectivity, and thermodynamic stabilization of the rate-determining step during the electrochemical CO_2RR. In this section, we focus on the main-group elements that support the CO_2RR as co-catalysts.

Li, Na, K, Rb, and Cs. Monovalent cations of alkali metals ($M1^+$), such as Li^+, Na^+, K^+, Rb^+, and Cs^+, typically participate as Lewis acids in the homogeneous electrochemical CO_2RR. A brief discussion of the stepwise CO_2 activation mechanism highlights the key effects of alkali metal cations on electrochemical CO_2 reduction chemistry. Herein, we consider the example of a chloro-iron(III)tetraphenylporphyrin (**$ClFe^{III}TPP$**, Fig. 8(A))-electrocatalyzed CO_2RR in the presence of Li^+ or Na^+.[2] The electrochemical data supported that adding Li^+ or Na^+ to a CO_2-saturated non-aqueous electrolyte enhanced the catalytic current in the presence of [**$Fe^{III}TPP$**]$^+$. The stepwise mechanism of the CO_2RR (Fig. 8(B)) indicated that **$ClFe^{III}TPP$** first underwent three sequential $1e^-$ reduction events to generate the [**Fe^0TPP**]$^{2-}$ species, which attached to CO_2 and formed a [**$Fe^{II}TPP$-CO_2**]$^{2-}$ adduct. In the presence of an alkyl metal ion ($M1^+$, such as Li^+ or Na^+), the O atom of the [**$Fe^{II}TPP$-CO_2**]$^{2-}$ adduct joined with $M1^+$ to form the intermediate **INT_1-M1**, followed by the binding of a second molecule of CO_2 to yield the intermediate **INT_2-M1** (Fig. 8(B)). The addition of another $M1^+$ to such an intermediate can produce a Li or Na carbonate salt, **$M1_2CO_3$**, as well as **$Fe^{II}TPP$-CO**. To complete the catalytic cycle, **$Fe^{II}TPP$-CO** was further reduced to regenerate [**Fe^ITPP**]$^-$ upon the formation of CO as the CO_2-reduced product. However, the primary role of $M1^+$ was to provide electrophilic assistance upon ion pairing with the [**$Fe^{II}TPP$-CO_2**]$^{2-}$ adduct to break (or weaken) the C–O bond of CO_2. Stronger Lewis acids were better at weakening the C–O bond in the [catalyst–CO_2] adduct, and higher turnover numbers were observed in the presence of Li^+ compared to that of the Na^+ ions. Overall, two moles of $M1^+$ were required to selectively reduce one mole of CO_2 to one mole of CO.

Effect of alkali metals in the rate-determining step of CO_2RR. Notably, the overall rates of CO_2RR using $M1^+$ ions were comparable to those measured for the same reaction using weak Brønsted acids, such as 1-propanol, 2,2,2-trifluoroethanol, and 2-pyrrolidone.[3,4] Furthermore, alkali metal ions could boost the rate of the CO_2 insertion into a transition metal–hydride bond during CO_2RR.[29] For example, the rate of CO_2 insertion into a Ru–hydride bond in a Ru complex bearing 2,2′-bipyridine and 2,2′:6′,2″-terpyridine chelating ligands was measured in the presence of Li^+, Na^+, K^+, or Rb^+, and the rate enhancement trend for the CO_2 insertion reaction was as follows: $Li^+ \gg Na^+ > K^+ > Rb^+$ (Table 2).[29] These observations suggested that monovalent alkali metal

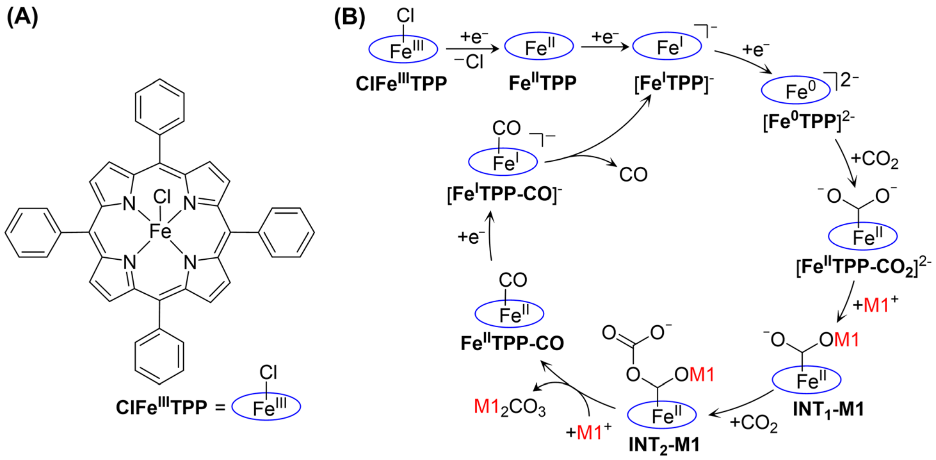

Fig. 8 (A) Structure of **ClFe^{III}TPP** for the electrochemical CO_2 reduction. (B) M1$^+$-assisted electrochemical CO_2-to-CO conversion. Adapted with the permission of ref. 2.

Table 2 Rate of CO_2 insertion reaction into an Ru–hydride bond of an Ru diimine complex in the presence of Li^+, Na^+, K^+, or Rb^+ in acetonitrile. Adapted with permission from ref. 29

Additive	Rate constant (M^{-2} s^{-1})
$LiNTF_2$[a]	3.1
LiOTf[b]	3.0
$LiBPh_4$[c]	3.0
$NaBAr^F{}_4$[d]	0.40
NaOTf	0.40
$NaBPh_4$	0.37
$NaNTF_2$	0.34
KPF_6	0.25
$KBPh_4$	0.21
$KNTf_2$	0.20
$RbBPh_4$	0.01

[a] NTf_2 = bis(trifluoromethane)sulfonamide. [b] OTf = trifluoromethanesulfonate. [c] BPh_4 = tetraphenylborate. [d] $BAr^F{}_4$ = tetrakis[3,5-bis(trifluoromethyl)phenyl]borate. Note: all rate constants are reported at room temperature.

ions with smaller sizes have more Lewis acidic character and thus, provide more stabilization to the rate-determining transition state during CO_2RR.

Role of alkali metals in CO_2RR selectivity. Alkali metal cations are often crucial for determining product selectivity in CO_2RR. For example, the CO_2RR performed using polycrystalline Au, Cu, and Ag electrodes in a pure sulfuric acid (H_2SO_4) electrolyte showed no CO production (primary C1 product in CO_2RR) without alkali metal cations.[30] This poor CO_2RR selectivity in the absence of alkali metal cations is likely due to the desolvated alkali metal cations building an electrostatic interaction with an O atom (or both O atoms) of the $CO_2{}^-$ intermediate after the [catalyst–CO_2] adduct formed. If these electrostatic interactions were not established during the CO_2RR, the selectivity toward CO formation would be poor. A model DFT calculation studied for the Au-electrode catalyzed CO_2RR in the presence of an alkali cation suggested that such electrostatic interactions could lower the Gibbs free energy of CO_2 adsorption (by at least 0.5 eV) at the electrode surface.[30] Additionally, the O–C–O bond angle decreased from 180° (linear) to below 140° (bent) when the [catalyst–CO_2] adduct was electrostatically stabilized by the alkali metal cations.[30] This change in CO_2 geometry during the CO_2RR often favors faster electron transfer from the electrode surface to CO_2, which was observed using the Cs^+ ion with Au electrodes.[30,31] Furthermore, the electrostatic interactions of metal cations and electrode surfaces could enhance the electric field at the interface of the electrode surface and bulk electrolyte, and the enhanced electric field could influence the adsorption of the $CO_2{}^-$ species at the electrode surface.[32–34] Consequently, higher adsorption of $CO_2{}^-$ at the electrodes, as well as subsequent proton-transfer events, could result in better product selectivity for CO_2RR.[35]

Role of alkali metals in CO_2RR kinetics. The rate of product formation relies on the nature of the monovalent cations, which is defined by the Lewis acidity of the alkali metal ions and their hydration number.[36,37] This hypothesis is supported by several reports, in that weakly hydrated Cs^+ and K^+ afforded high current densities during electrochemical CO_2RR in the aqueous electrolytes, regardless of the pH.[34,37,38] Electrochemical CO_2RR using gas diffusing electrodes further supported that high partial current densities for CO production were observed in the presence of alkali metal cations in the order of $Cs^+ > K^+ > Na^+ > Li^+$.[39–42] However, the concentration of these alkali metal solutions should be low enough, <1.0 M, to avoid the background bicarbonate reduction promoted by the cations.[43]

Mg, Ca, and Ba. The Lewis acidities of alkaline-earth metals can influence the electrochemical CO_2RR, similar to the above-mentioned discussion for alkali metals; however, they follow different CO_2RR pathways than that for the alkali metal-assisted CO_2RR. The dicationic forms of three alkaline earth metals ($M2^{2+}$), Mg^{2+}, Ca^{2+}, and Ba^{2+}, are known to enhance CO_2RR rates.[2] Herein, we focus on the stabilization strategies of the [catalyst–CO_2] adduct in the presence of $M2^{2+}$ ions and how such strategies differ from those observed in M1$^+$-supported [catalyst–CO_2] adduct stabilization. For further discussion, we chose the example of the **ClFe^{III}TPP**-catalyzed CO_2RR and examined the effects of $M2^{2+}$ ions on the stabilization of the **[Fe^{II}TPP-CO$_2$]$^{2-}$** adduct during the CO_2RR (Fig. 9). As shown in Fig. 8(B), stabilization of the **[Fe^{II}TPP-CO$_2$]$^{2-}$** adduct is crucial for the CO_2RR. Therefore, we discuss two different strategies followed by the $M2^{2+}$ ions (paths A and B in Fig. 9) to stabilize the **[Fe^{II}TPP-CO$_2$]$^{2-}$** adduct. Following path A, a single $M2^{2+}$ ion could interact with both O atoms of **[Fe^{II}TPP-CO$_2$]$^{2-}$** electrostatically, forming the intermediate **INT1-M2**. Eventually, the second molecule of CO_2 reacted with **INT1-M2** to produce metal carbonate salts ($M2CO_3$) and CO products. In contrast, if $M2^{2+}$ interacted with only one O atom of **[Fe^{II}TPP-CO$_2$]$^{2-}$** following path B (Fig. 9), an **INT2-M2** intermediate was formed. **INT2-M2** was then reduced using a weak Brønsted acid to generate formate (HCO_2^-) as the final CO_2-reduced product. A mixture of products was often obtained from the CO_2RR in the presence of $M2^{2+}$ ions. For example, 70% CO and 30% HCO_2^- were obtained *via* the CO_2RR using **[Fe^{III}TPP]$^+$** in the presence of Mg^{2+}. Furthermore, these experiments were repeated using two different $M2^{2+}$ ions, Ca^{2+} and Ba^{2+}, to compare the overall rate of the CO_2RR. A similar apparent rate constant, 1.5×10^4 M^{-2} s^{-1}, was estimated for Mg^{2+} and Ca^{2+}, which was comparatively higher than that observed in the presence of Ba^{2+} (3.0×10^3 M^{-2} s^{-1}).[2] However, the first-order reaction in $M2^{2+}$ concentration was observed for the CO_2RR, indicating that only one mole of $M2^{2+}$ was sufficient to complete the CO_2RR cycle, whereas the order of the reaction was 2 when alkali metal ions, $M1^+$, were used. This suggests that smaller equivalents of $M2^{2+}$ ions can effectively enhance the CO_2RR selectivity.

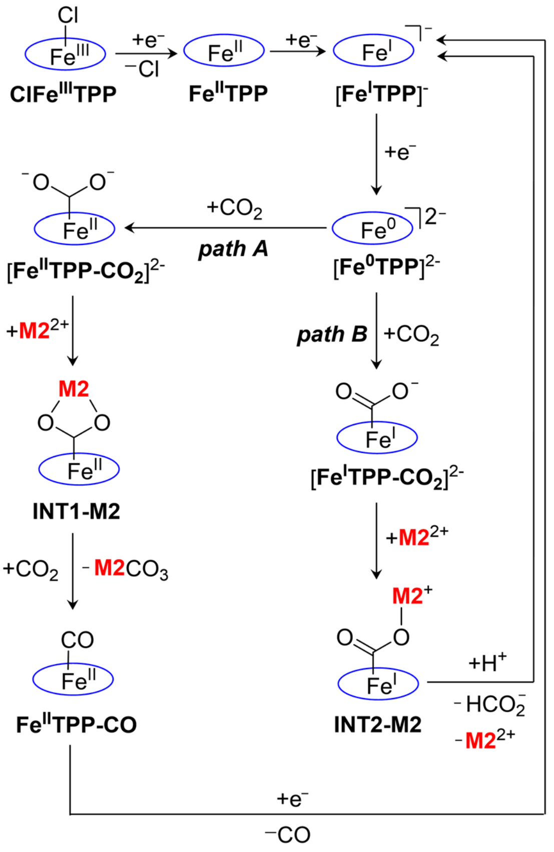

Fig. 9 Mg^{2+}, Ca^{2+}, or Ba^{2+}-assisted electrochemical CO_2-to-CO conversion catalyzed by **ClFe^{III}TPP**. Adapted with the permission of ref. 2.

Further molecular evidence of the [catalyst–CO_2–$M2^{2+}$] intermediate formation in the CO_2RR cycle was revealed using cobalt phthalocyanine (CoPc)-modified Au electrodes in the presence of Mg^{2+} (Fig. 10(A)).[44] CV data revealed that these CoPc-modified Au electrodes exhibited high catalytic currents with approximately 80% FE for CO formation when 0.05 M of Mg^{2+} ions were present in a CO_2-saturated 0.1 M $KHCO_3$ electrolyte. Scanning tunneling microscopy (STM) images were captured for the CoPc monolayer on the electrode surface following CO_2 adsorption, and the apparent thickness of the layer was estimated to be ~0.15 nm. The thickness increased to ~0.19 nm when STM images were taken for the same in CO_2-saturated $Mg(ClO_4)_2$ solution,[44] indicating Mg^{2+} ions were networked to the CoPc–CO_2 complex on the surface *via* electrostatic interactions. Additionally, high-resolution STM images collected after performing CO_2RR at −1.1 V *vs.* saturated calomel electrode (SCE) showed only the presence of the Co atom and phthalocyanine macrocycle, without the existence of Mg^{2+}, further confirming that Mg^{2+} assisted in stabilizing the [CoPc–CO_2] adduct without getting adsorbed onto the electrode surface. Notably, when similar CO_2RR processes were performed using CoPc-modified Au electrodes in different alkaline-earth metal electrolytes, such as $Ca(ClO_4)_2$ and $Ba(ClO_4)_2$, the apparent layer height of the CoPc monolayer was similar to that observed in the CO_2- and $M2^{2+}$-free solutions after saturation with CO_2. These data further highlight that Mg^{2+} ions play a unique role in supporting CO_2 binding at the active center of the catalyst. To gain more insight into the effect of Mg^{2+} on CO_2 adsorption and binding to the catalytic center, *in situ* electrochemical STM (ECSTM) was performed for an identical CoPc-modified electrode, and the surface coverage of the adsorbed CO_2 onto the catalyst-immobilized electrode was estimated. In the CO_2-saturated $Mg(ClO_4)_2$ electrolyte, the average surface coverage was approximately 30% (Fig. 10(B)), which was much lower when the electrolyte was changed to $NaClO_4$ (12.6%), $Ca(ClO_4)_2$ (17%), or $Ba(ClO_4)_2$ (14.4%). Furthermore, the rate constant of CO_2 adsorption in the $Mg(ClO_4)_2$ solution was 0.36 min^{-1}, which was higher than that in the Mg^{2+}-free solution (0.26 min^{-1}). In contrast, the rate of CO_2 desorption from the surface was 0.89 min^{-1} in the presence of Mg^{2+}, compared with 1.77 min^{-1} in the Mg^{2+}-free electrolyte. Additional calculations of the ΔG for the formation of CoPc–CO_2 and CoPc–CO_2–Mg^{2+} complexes indicated that CoPc–CO_2–Mg^{2+} (ΔG = −0.142 eV) was more thermodynamically stable than the CoPc–CO_2 complex (ΔG = −0.038 eV). Together, these results indicate that Mg^{2+} acts as an efficient stabilizer to increase the CO_2 adsorption/binding rate at the catalyst active site(s), thereby influencing the overall CO_2RR kinetics.

B. B-centered catalysts are not commonly used for CO_2RR catalysis, except in a few reports in which B acts as a dopant.

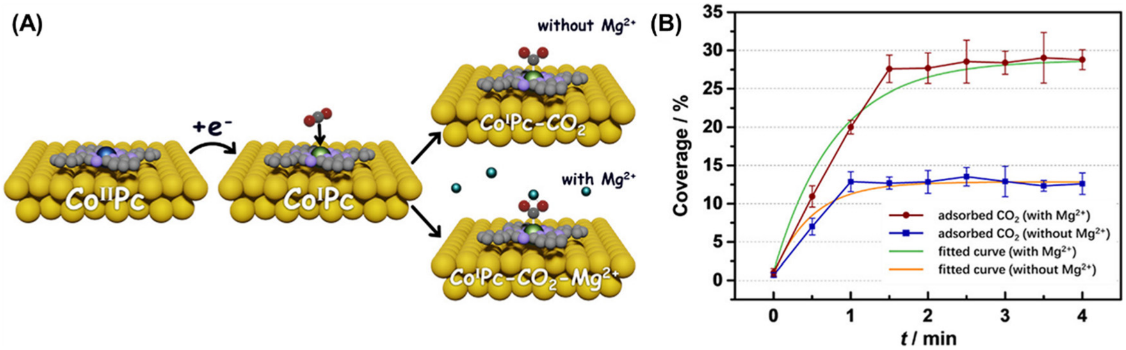

Fig. 10 (A) CoPc-modified Au electrodes, and the proposed steps to form CoPc–CO_2 and CoPc–CO_2–Mg^{2+} complexes. (B) Surface coverage estimated based on *in situ* electrochemical STM and simulated data for CO_2 binding with and without Mg^{2+} ions. Adapted with the permission of ref. 44.

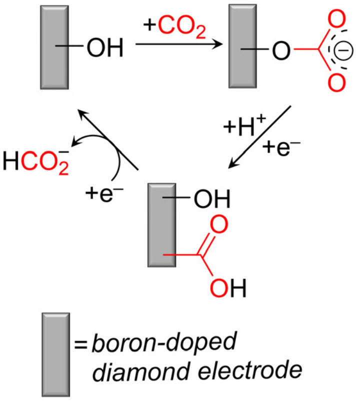

Fig. 11 Proposed steps for the electrochemical CO_2RR using B-doped diamond electrodes (BDDEs). Adapted with the permission of ref. 45.

One example is a B-doped diamond electrode (BDDE), which alters the electrochemical CO_2RR pathway by avoiding the typical generation of $CO_2^{\bullet-}$ in the elementary CO_2RR step.[45] In the CO_2RR pathway promoted by BDDEs, CO_2 binds to the electrode surface as monodentate carbonate, [BDDE–O–CO_2^{2-}] (Fig. 11), instead of forming the [BDDE–CO_2] adduct in the CO_2-saturated aqueous electrolyte. *In situ* attenuated total reflectance infrared (ATR-IR) spectroscopy confirmed the presence of the carbonate group at the BDDE surface, with strong absorption peaks at 1530–1470 and 1370–1300 cm^{-1} due to the vibration of –O–CO_2.[45] Notably, the intensity of these ATR-IR absorption peaks increased with time as more CO_2 was adsorbed at the electrode surface upon saturation with CO_2. This CO_2 activation at the BDDE is termed the ''self-activation'' process, which increases the effective electroactive area toward CO_2RR.[45] Next, those carbonate moieties at the BDDE were converted to carboxylic groups following a proton-coupled electron transfer (PCET) step and finally to formate, which was released as a CO_2-reduced product. The electrical-to-chemical energy conversion efficiency for CO_2RR using the BDDE was 50% for the production of formate (or formic acid, depending on the pH of the solution) from CO_2. Although the actual role of immobilized B in BDDE is yet to be explored, B-doped electrodes could be promising for generating formate from CO_2 *via* selective carbonate intermediates.

Another example of a B-supported electrochemical CO_2RR was reported by Liu *et al.*, in which they introduced B into a single atomic Fe site complex.[46] Using a B-incorporated single atomic Fe electrocatalyst, ~99% FE for CO production with a current density of 130 mA cm^{-2} was observed in CO_2-saturated 0.1 M $KHCO_3$ buffer after performing bulk electrolysis in a membrane-separated H-cell. Under these electrochemical conditions, the presence of B near the Fe active site in the single-Fe-atom complex enhanced the reaction kinetics for the overall CO_2RR. Furthermore, the investigation of double-layered capacitance revealed that the presence of B enhanced the effective electrochemical surface area of the B-supported single Fe atom electrodes and exposed more active sites, resulting in better electrode–CO_2 interaction.[46] Thus, faster CO_2RR kinetics were obtained using the B-incorporated single Fe atom electrocatalysts.

Ga. CO is a common C_1 product in the electrochemical CO_2RR cycle; however, using Ga in catalysts has been primarily reported for producing more value-added products, such as methane (CH_4), formic acid (HCOOH), ethane (C_2H_6), ethylene (C_2H_4), *n*-propanol (C_3H_7OH), and methylglyoxal (CH_3CO-CHO).[47–49] In this section, we discuss these examples and the role of Ga in electrocatalytic CO_2RR cycles.

Sekimoto *et al.* demonstrated the performance of Sn- or Si-doped Ga oxide (Ga_2O_3) electrodes for the selective production of HCOOH with >80% FE in the electrochemical CO_2RR.[47] The authors revealed that the FE for HCOOH formation was independent of the type of dopant (Sn or Si) present in the Ga_2O_3 electrodes. Therefore, the selective CO_2RR toward the formation of only HCOOH could be credited to the performance of the Ga_2O_3 electrodes. Thermodynamic insights into HCOOH formation at the Ga_2O_3 electrodes were also obtained using DFT. Protonation occurred at the C center following CO_2 adsorption on the Ga_2O_3 surface, yielding the [HCOO–Ga_2O_3] adduct, in which the two O atoms coordinated with the Ga sites. The distance between one Ga atom and one O atom was 0.20 nm, and such weak binding could help the desorption of the product (such as HCOOH) after [HCOO–Ga_2O_3] was reduced by a single H^+ and single e^-. Furthermore, the Ga_2O_3

electrodes exhibited stable catalytic current ($\sim$0.3 mA cm^{-2}) over 50 repeating CV sweeps recorded under CO_2 atmosphere, indicating the robust stability of Ga electrodes for CO_2RR.

Lewis *et al.* determined that bimetallic NiGa films (NiGa, Ni_3Ga, and Ni_5Ga_3) were active electrocatalytic materials for the CO_2RR in a neutral bicarbonate solution.[48] Using NiGa films, CH_4, C_2H_6, and C_2H_4 were obtained as the primary CO_2-reduced products at low onset potentials, with less than −0.48 V *vs.* reversible hydrogen electrode (RHE).[48] Furthermore, various NiGa films catalyzed the formation of CO_2-reduced C_2 products *via* an intermediate CO formation step. Further reduction of the CO with selective H^+ and e^- yielded CH_4 and C_2 products. CO could bind strongly to the Ni center,[50] but the presence of Ga in bimetallic NiGa films destabilized Ni–CO interactions, resulting in the further reduction of CO toward more reduced products, such as CH_4 or the multi-carbon products C_2H_4 and C_2H_6.

Other than Ga-based electrodes, single-atom Ga electrocatalysts were reported for the selective CO_2-to-CO conversion with FEs $>$90%.[51] Using these single-atom Ga catalysts, much higher current densities were obtained for the electrochemical CO_2RR compared to the previously discussed Ga_2O_3 electrodes. Based on the DFT calculations, the adsorbed CO_2 was protonated at the rate-determining step to form the [Ga electrode–COOH] intermediate, which finally generated CO upon further reduction. Furthermore, doping single-atom Ga electrodes with heteroatoms (*e.g.*, P and S) significantly decreased the ΔG barriers for the rate-determining step of CO generation. The P- and S-doped, single-atom Ga electrocatalysts were flexible in geometry at the Ga center, which also supported the thermodynamic parameters of the CO formation step by reducing the activation energy of the *COOH species generated at the surface of the electrode.

Ge and Sn. Group 14 elements rarely serve as catalytic centers for multi-H^+/multi-e^- transfer reactions, except for a few examples of Ge- or Sn-based solid materials. For example, Ge–S–In amorphous glass materials[52] and Sn-containing electrocatalysts[53] have been reported for the CO_2RR owing to their high selectivity, low overpotential, and steady catalytic stability.

Ge. Ge–S–In chalcogenide glass materials were prepared to perform CO_2RR in an aqueous electrolyte.[52] Using these Ge–S–In glass electrodes, $\sim$15% FE for CO formation at an applied potential of −1.3 V *vs.* normal hydrogen electrode (NHE) was determined after performing bulk electrolysis for over 5 h. Notably, when the micron-sized particles of Ge–S–In were deposited onto the C-paper electrode, a comparatively higher catalytic current was observed in the CO_2-saturated aqueous electrolyte. Upon performing preparative-scale electrolysis using micron-sized Ge–S–In particles adsorbed onto the C-paper, the product in the CO_2RR changed to HCOOH with an FE of 26.1%. Further control electrolysis without drop-casting Ge–S–In particles on the C-paper electrodes exhibited a low FE (7.1%) for HCOOH, indicating that Ge–S–In materials are required to increase the FE for HCOOH production.

Sn. Publications on Sn-based electrocatalytic materials for CO_2RR have grown since 2014.[53] Among them, metallic Sn-based catalysts have been promising for electrochemical CO_2RR, owing to their high surface area that enables more interaction between the catalyst and CO_2.[54] The enhanced interaction reduces overpotentials, thus thermodynamically proceeding in the formation of CO_2-reduced intermediates, COOH* or HCOO*.[55] Furthermore, different morphologies of metallic Sn electrodes, such as rod, planar sheet, and dendritic, have been tested to optimize the size and shape of the Sn electrodes with their efficiency and product selectivity toward CO_2RR. Moreover, the nanorod-shaped Sn electrodes selectively generated HCOOH with an FE of 94.5% at the applied potential of −1.6 V *vs.* Ag/AgCl.[56] Sn-containing bimetallic electrocatalysts, such as Pd–Sn,[57] Cu–Sn,[58] and Bi–Sn,[59] have also been studied for the CO_2RR, where HCO_2^- or HCOOH is the major product. Additionally, Cu–Sn alloys are known for selective CO_2-to-CO conversion in CH_3CN electrolytes, as reported by Sacci *et al.*[60]

In addition to the Sn-based materials discussed above, Sn oxide electrodes have been extensively explored. For example, Sn oxide nanoparticles immobilized onto graphene layers promoted the CO_2RR at only 340 mV of overpotential with $>$93% FE for HCO_2^- formation. These electrocatalysts were stable over 18 h. Moreover, one-dimensional Sn oxide nanomaterials exhibited elevated electrochemical CO_2RR performance, such as high current densities and selective product formation (commonly HCOOH formation).[61] These remarkable CO_2RR activities are primarily attributed to the large surface area at the catalyst site, which enhances the catalyst–substrate interaction.

P and Bi. Group 15 elements, primarily P and Bi, are commonly used as co-catalysts in redox reactions related to small-molecule activation. Herein, we chose examples of reports that emphasize the roles of P and Bi in influencing the thermodynamic and kinetic parameters of the CO_2RR.

P. P typically assists the transition-metal-based catalysts for CO_2RR.[62] For example, the presence of P near a single-Fe-atom catalyst has prompted the CO_2RR catalysis toward the selective formation of CO with an FE of 98% and TOF of 508.8 h^{-1} at the overpotential of 0.34 V.[62] When P was near the single Fe atom, the partial current densities for CO production was enhanced, and the overpotential for the overall CO_2RR decreased by the Fe site stabilizing at a lower oxidation state upon the formation of *COOH and *CO intermediates. Thus, the reduced Fe site could push more electron densities to activate CO_2 and enabled CO desorption at the end of the catalytic cycle, as determined by DFT calculations.[62] Furthermore, similar developments of catalytic materials by incorporating P into an N-doped, C-supported single-Fe-atom catalyst, reported by Sun *et al.*, demonstrated that 97% FE can be obtained for CO formation at 0.32 V of overpotential while performing CO_2RR in the aqueous electrolyte.[63] DFT calculations were in agreement; therefore, the presence of P atoms near the Fe center can support more electron localization at the Fe center, thus stabilizing the *COOH intermediate.

Cu nanocrystal catalysts doped with P have also become efficient electrocatalysts for converting CO_2 into ethylene

(FE, ~31%) and alcohols (~45%).[64] The catalytic current density achieved in the CO_2RR was high (57.2 mA cm^{-2}) compared to that for the Cu catalysts without P-doping. However, the formation of C_{2+} products from CO_2 critically depends on the thermodynamic landscape behind C–C bond formation. Chen *et al.* estimated that the ΔG for C–C coupling processes was more challenging ($\Delta G = 0.51$ eV) without P ($\Delta G = -0.49$ eV). They further reported that the presence of P atoms near Cu atoms could influence the energy levels of the Cu 3d-orbitals, bringing them near the Fermi level and facilitating a stronger overlap between the 3d-orbitals of P-doped Cu and the reduced CO_2 intermediates (*i.e.*, *COHCO). Thus, these intermediates were energetically stabilized at the surface of the P-doped Cu electrodes, lowering the overpotential of the reaction.

In addition to transition metals, the introduction of P into N-doped C catalysts (N–C) also exhibited notable effects on the electrochemical CO_2RR. Li *et al.* studied metal-free C electrodes co-doped with P and N and determined their stability over 24 h of electrolysis while reducing CO_2 to CO with an FE of 92%.[65] DFT calculations further supported the hypothesis that the P dopant could lower the ΔG of *COOH formation and polarize the electron densities at the active site to raise the energy level near the Fermi level. This change in the energy level significantly boosted the electron-transfer process between the active site of the catalyst and CO_2 (or reduced CO_2 intermediates).

Bi. B-containing electrocatalysts for CO_2RR are often selective for the reduction of CO_2 to HCO_2^-. Here, we focus on Bi nanomaterials and B-doped Bi electrodes for the CO_2RR. Fan *et al.* revealed that the curvature of Bi nanomaterials, such as Bi nanotubes and nanosheets, could influence the thermodynamic landscape of the CO_2RR and product selectivity.[66] This hypothesis was investigated using Bi nanotubes with high curvature, and the catalytic current density for CO_2RR was 39.4 mA cm^{-2} with 97% selectivity toward HCO_2^- production. Compared with the performance of Bi nanosheets under identical electrochemical conditions, Bi nanotubes were more effective in maintaining a high FE (>90%) for HCO_2^- formation at a fixed applied potential.

An additional example of Bi-based materials for the selective CO_2-to-HCO_2^- conversion was reported by Liu *et al.*[67] They prepared B-doped Bi-based electrodes and achieved 90% FE for the HCO_2^- formation reaction within a wider applied potential window between −0.6 and −1.2 V *vs.* RHE. The incorporation of B into Bi materials enriched the electron density of Bi and altered the adsorption energy of the CO_2-reduced intermediate, OCHO*. These effects influenced the kinetics of the CO_2RR. However, Bi materials, which are less toxic, earth-abundant, and environmentally friendly, are promising for the selective CO_2-to-HCO_2^- conversion.

Summary

Electrochemical HER and CO_2RR have gained significant attention for addressing climate change and future energy infrastructure. Electrocatalytic conversion is promising in the field of chemistry, where transition-metal catalysts are in the spotlight. Despite the remarkable progress in the development of transition-metal-based electrocatalysts, electrocatalytic materials comprising main-group elements have potential for converting CO_2 into value-added chemicals or producing H_2. This article reviewed studies that explored the main-group element-based electrocatalysts for the CO_2RR and HER. We discussed the activities of the main-group elements by carefully selecting elements that exhibit unique roles in enhancing the CO_2RR or HER kinetics, product selectivity, or assisting in the intermediate stabilization steps. First, we discussed the remarkably efficient HER activities promoted by the molecular Al- and Ga-based electrocatalysts and their mechanism for producing H_2, resembling the pathways of the transition-metal-catalyzed HER. Next, we highlighted the performance of Ge and Sn materials for the CO_2RR and HER, including one of our studies that used a molecular Sn porphyrin derivative that produces H_2 in a non-aqueous electrolyte. Second, we discussed the selectivity of CO_2-to-HCO_2^- using group 13 elements, particularly B and Ga. Additionally, we focused on the Lewis acidity of the elements in groups 1 and 2 toward CO_2RR selectivity and kinetics. Finally, we discussed the various roles of P, Sb, and Bi in CO_2RR and HER electrocatalysis under both homogeneous and heterogeneous conditions. Together, the exclusive discussion on the main-group element-promoted CO_2RR and HER could serve as excellent resources for progressing main-group element-based electrocatalyst design, development, and implementation in fuel-forming reactions or storing energies in chemical bonds.

Conflicts of interest

There are no conflicts to declare.

Acknowledgements

This study was supported by the National Science Foundation (grant no. CHE-2041436).

References

1 P. P. Power, *Nature*, 2010, **463**, 171–177.
2 I. Bhugun, D. Lexa and J.-M. Savéant, *J. Phys. Chem.*, 1996, **100**, 19981–19985.
3 I. Bhugun, D. Lexa and J.-M. Savéant, *J. Am. Chem. Soc.*, 1996, **118**, 1769–1776.
4 I. Bhugun, D. Lexa and J.-M. Savéant, *J. Am. Chem. Soc.*, 1994, **116**, 5015–5016.
5 S. Sinha, M. S. Aaron, J. Blagojevic and J. J. Warren, *Chem. – Eur. J.*, 2015, **21**, 18072–18075.
6 M. N. Jackson and Y. Surendranath, *Acc. Chem. Res.*, 2019, **52**, 3432–3441.
7 C. K. Williams, G. A. McCarver, A. Chaturvedi, S. Sinha, M. Ang, K. D. Vogiatzis and J. Jiang, *Chem. – Eur. J.*, 2022, **28**, e202201323.
8 A. Chaturvedi, G. A. McCarver, S. Sinha, E. G. Hix, K. D. Vogiatzis and J. Jiang, *Angew. Chem., Int. Ed.*, 2022, **61**, e202206325.
9 S. Sinha, C. K. Williams and J. Jiang, *iScience*, 2022, **25**, 103628.
10 S. Amanullah, P. Saha, A. Nayek, M. E. Ahmed and A. Dey, *Chem. Soc. Rev.*, 2021, **50**, 3755–3823.

11 N. S. Lewis and D. G. Nocera, *Proc. Natl. Acad. Sci. U. S. A.*, 2006, **103**, 15729–15735.

12 G. Ménard and D. W. Stephan, *J. Am. Chem. Soc.*, 2010, **132**, 1796–1797.

13 A. E. Ashley and D. O'Hare, in *Frustrated Lewis Pairs II*, ed. G. Erker and D. W. Stephan, Springer Berlin Heidelberg, Berlin, Heidelberg, 2012, vol. 334, pp. 191–217.

14 B. L. Thompson and Z. M. Heiden, *Tetrahedron*, 2019, **75**, 2099–2105.

15 E. J. Thompson and L. A. Berben, *Angew. Chem., Int. Ed.*, 2015, **54**, 11642–11646.

16 T. J. Sherbow, J. C. Fettinger and L. A. Berben, *Inorg. Chem.*, 2017, **56**, 8651–8660.

17 J. L. Dempsey, B. S. Brunschwig, J. R. Winkler and H. B. Gray, *Acc. Chem. Res.*, 2009, **42**, 1995–2004.

18 M. L. Helm, M. P. Stewart, R. M. Bullock, M. R. DuBois and D. L. DuBois, *Science*, 2011, **333**, 863–866.

19 S. Sinha, G. N. Tran, H. Na and L. M. Mirica, *Chem. Commun.*, 2022, **58**, 1143–1146.

20 N. Wang, H. Lei, Z. Zhang, J. Li, W. Zhang and R. Cao, *Chem. Sci.*, 2019, **10**, 2308–2314.

21 J. Radhakrishnan, A. Kareem, S. Senthilkumar and K. Biswas, *J. Alloys Compd.*, 2022, **917**, 165444.

22 J. Jiang, K. L. Materna, S. Hedström, K. R. Yang, R. H. Crabtree, V. S. Batista and G. W. Brudvig, *Angew. Chem., Int. Ed.*, 2017, **56**, 9111–9115.

23 W.-C. Xiao, Y.-W. Tao and G.-G. Luo, *Int. J. Hydrogen Energy*, 2020, **45**, 8177–8185.

24 P. Liu, J. A. Rodriguez, T. Asakura, J. Gomes and K. Nakamura, *J. Phys. Chem. B*, 2005, **109**, 4575–4583.

25 S. T. Oyama, T. Gott, H. Zhao and Y.-K. Lee, *Catal. Today*, 2009, **143**, 94–107.

26 H. Gerischer, A. Mauerer and W. Mindt, *Surf. Sci.*, 1966, **4**, 431–439.

27 R. Memming and G. Neumann, *J. Electroanal. Chem. Interfacial Electrochem.*, 1969, **21**, 295–305.

28 Y. M. Wu, W. S. Li, X. M. Long, F. H. Wu, H. Y. Chen, J. H. Yan and C. R. Zhang, *J. Power Sources*, 2005, **144**, 338–345.

29 J. E. Heimann, W. H. Bernskoetter and N. Hazari, *J. Am. Chem. Soc.*, 2019, **141**, 10520–10529.

30 G. Marcandalli, M. C. O. Monteiro, A. Goyal and M. T. M. Koper, *Acc. Chem. Res.*, 2022, **55**, 1900–1911.

31 B. Huang, K. H. Myint, Y. Wang, Y. Zhang, R. R. Rao, J. Sun, S. Muy, Y. Katayama, J. Corchado Garcia, D. Fraggedakis, J. C. Grossman, M. Z. Bazant, K. Xu, A. P. Willard and Y. Shao-Horn, *J. Phys. Chem. C*, 2021, **125**, 4397–4411.

32 L. D. Chen, M. Urushihara, K. Chan and J. K. Nørskov, *ACS Catal.*, 2016, **6**, 7133–7139.

33 G. Hussain, L. Pérez-Martínez, J.-B. Le, M. Papasizza, G. Cabello, J. Cheng and A. Cuesta, *Electrochim. Acta*, 2019, **327**, 135055.

34 S. Ringe, E. L. Clark, J. Resasco, A. Walton, B. Seger, A. T. Bell and K. Chan, *Energy Environ. Sci.*, 2019, **12**, 3001–3014.

35 J. Resasco, L. D. Chen, E. Clark, C. Tsai, C. Hahn, T. F. Jaramillo, K. Chan and A. T. Bell, *J. Am. Chem. Soc.*, 2017, **139**, 11277–11287.

36 M. C. O. Monteiro, F. Dattila, N. López and M. T. M. Koper, *J. Am. Chem. Soc.*, 2022, **144**, 1589–1602.

37 M. C. O. Monteiro, F. Dattila, B. Hagedoorn, R. García-Muelas, N. López and M. T. M. Koper, *Nat. Catal.*, 2021, **4**, 654–662.

38 M. R. Singh, Y. Kwon, Y. Lum, J. W. Ager and A. T. Bell, *J. Am. Chem. Soc.*, 2016, **138**, 13006–13012.

39 B. Endrődi, A. Samu, E. Kecsenovity, T. Halmágyi, D. Sebők and C. Janáky, *Nat. Energy*, 2021, **6**, 439–448.

40 M. C. O. Monteiro, M. F. Philips, K. J. P. Schouten and M. T. M. Koper, *Nat. Commun.*, 2021, **12**, 4943.

41 M. R. Thorson, K. I. Siil and P. J. A. Kenis, *J. Electrochem. Soc.*, 2013, **160**, F69–F74.

42 S. S. Bhargava, F. Proietto, D. Azmoodeh, E. R. Cofell, D. A. Henckel, S. Verma, C. J. Brooks, A. A. Gewirth and P. J. A. Kenis, *ChemElectroChem*, 2020, **7**, 2001–2011.

43 G. Marcandalli, A. Goyal and M. T. M. Koper, *ACS Catal.*, 2021, **11**, 4936–4945.

44 Y.-Q. Wang, X.-H. Dan, X. Wang, Z.-Y. Yi, J. Fu, Y.-C. Feng, J.-S. Hu, D. Wang and L.-J. Wan, *J. Am. Chem. Soc.*, 2022, **144**, 20126–20133.

45 J. Du, A. Fiorani, T. Inagaki, A. Otake, M. Murata, M. Hatanaka and Y. Einaga, *JACS Au*, 2022, **2**, 1375–1382.

46 S. Liu, M. Jin, J. Sun, Y. Qin, S. Gao, Y. Chen, S. Zhang, J. Luo and X. Liu, *Chem. Eng. J.*, 2022, **437**, 135294.

47 T. Sekimoto, M. Deguchi, S. Yotsuhashi, Y. Yamada, T. Masui, A. Kuramata and S. Yamakoshi, *Electrochem. Commun.*, 2014, **43**, 95–97.

48 D. A. Torelli, S. A. Francis, J. C. Crompton, A. Javier, J. R. Thompson, B. S. Brunschwig, M. P. Soriaga and N. S. Lewis, *ACS Catal.*, 2016, **6**, 2100–2104.

49 T. Chen, J. Hu, K. Wang, K. Wang, G. Gan and J. Shi, *Energy Fuels*, 2021, **35**, 17784–17790.

50 Y. Hori and A. Murata, *Electrochim. Acta*, 1990, **35**, 1777–1780.

51 Z. Zhang, J. Zhu, S. Chen, W. Sun and D. Wang, *Angew. Chem., Int. Ed.*, 2023, **62**, e202215136.

52 F. S. Khan, M. Sugiyama, K. Fujii, Yu. S. Tver'yanovich and Y. Nakano, *Heliyon*, 2020, **6**, e03513.

53 N. S. Shaikh, J. S. Shaikh, V. Márquez, S. C. Pathan, S. S. Mali, J. V. Patil, C. K. Hong, P. Kanjanaboos, O. Fontaine, A. Tiwari, S. Praserthdam and P. Praserthdam, *Mater. Today Sustain.*, 2023, 100384.

54 X. Zheng, P. De Luna, F. P. García de Arquer, B. Zhang, N. Becknell, M. B. Ross, Y. Li, M. N. Banis, Y. Li, M. Liu, O. Voznyy, C. T. Dinh, T. Zhuang, P. Stadler, Y. Cui, X. Du, P. Yang and E. H. Sargent, *Joule*, 2017, **1**, 794–805.

55 J. S. Yoo, R. Christensen, T. Vegge, J. K. Nørskov and F. Studt, *ChemSusChem*, 2016, **9**, 358–363.

56 V. S. K. Yadav, Y. Noh, H. Han and W. B. Kim, *Catal. Today*, 2018, **303**, 276–281.

57 X. Bai, W. Chen, C. Zhao, S. Li, Y. Song, R. Ge, W. Wei and Y. Sun, *Angew. Chem., Int. Ed.*, 2017, **129**, 12387–12391.

58 Y. Wang, Y. Chen, Y. Zhao, J. Yu, Z. Liu, Y. Shi, H. Liu, X. Li and W. Zhou, *Appl. Catal., B*, 2022, **307**, 120991.

59 B. Ren, G. Wen, R. Gao, D. Luo, Z. Zhang, W. Qiu, Q. Ma, X. Wang, Y. Cui, L. Ricardez–Sandoval, A. Yu and Z. Chen, *Nat. Commun.*, 2022, **13**, 2486.

60 R. Sacci, S. Velardo, L. Xiong, D. Lutterman and J. Rosenthal, *Energies*, 2019, **12**, 3132.

61 B. Kumar, V. Atla, J. P. Brian, S. Kumari, T. Q. Nguyen, M. Sunkara and J. M. Spurgeon, *Angew. Chem., Int. Ed.*, 2017, **56**, 3645–3649.

62 K. Li, S. Zhang, X. Zhang, S. Liu, H. Jiang, T. Jiang, C. Shen, Y. Yu and W. Chen, *Nano Lett.*, 2022, **22**, 1557–1565.

63 X. Sun, Y. Tuo, C. Ye, C. Chen, Q. Lu, G. Li, P. Jiang, S. Chen, P. Zhu, M. Ma, J. Zhang, J. H. Bitter, D. Wang and Y. Li, *Angew. Chem., Int. Ed.*, 2021, **133**, 23806–23810.

64 H. Chen, Z. Wang, X. Wei, S. Liu, P. Guo, P. Han, H. Wang, J. Zhang, X. Lu and B. Wei, *Appl. Surf. Sci.*, 2021, **544**, 148965.

65 S. Chen, T. Liu, S. O. Olanrele, Z. Lian, C. Si, Z. Chen and B. Li, *J. Energy Chem.*, 2021, **54**, 143–150.

66 K. Fan, Y. Jia, Y. Ji, P. Kuang, B. Zhu, X. Liu and J. Yu, *ACS Catal.*, 2020, **10**, 358–364.

67 X. Chen, H. Chen, W. Zhou, Q. Zhang, Z. Yang, Z. Li, F. Yang, D. Wang, J. Ye and L. Liu, *Small*, 2021, **17**, 2101128.